
SPACE: SPike-Aware Consistency Enhancement for Test-Time Adaptation in Spiking Neural Networks

Xinyu Luo Kecheng Chen Pao-Sheng Vincent Sun Chris XING TIAN
Arindam Basu Haoliang Li

City University of Hong Kong
xinyuluo8-c@my.cityu.edu.hk

Abstract

Spiking Neural Networks (SNNs), as a biologically plausible alternative to Artificial Neural Networks (ANNs), have demonstrated advantages in terms of energy efficiency, temporal processing, and biological plausibility. However, SNNs are highly sensitive to distribution shifts, which can significantly degrade their performance in real-world scenarios. Traditional test-time adaptation (TTA) methods designed for ANNs often fail to address the unique computational dynamics of SNNs, such as sparsity and temporal spiking behavior. To address these challenges, we propose SPike-Aware Consistency Enhancement (SPACE), the first source-free and single-instance TTA method specifically designed for SNNs. SPACE leverages the inherent spike dynamics of SNNs to maximize the consistency of spike-behavior-based local feature maps across augmented versions of a single test sample, enabling robust adaptation without requiring source data. We evaluate SPACE on multiple datasets. Furthermore, SPACE exhibits robust generalization across diverse network architectures, consistently enhancing the performance of SNNs on CNNs (such as VGG and ResNet), Transformer models, and ConvLSTM architectures. Experimental results show that SPACE outperforms state-of-the-art methods, highlighting its effectiveness and robustness in real-world settings.

1 Introduction

Recent advancements in neuroscience-inspired computing have placed Spiking Neural Networks (SNNs) at the forefront of research as a biologically plausible alternative to traditional Artificial Neural Networks (ANNs). While ANNs have achieved remarkable success in various domains, their reliance on dense, black-box architectures often limits their interpretability and energy efficiency. In contrast, SNNs emulate the sparse, event-driven dynamics of biological neurons, providing several advantages in terms of computational efficiency, temporal processing, and explainability [4, 12, 37]. However, the unique features that make SNNs advantageous—such as their reliance on temporal information and sparse spiking—also pose significant challenges in dynamic real-world environments. SNNs encode information dynamically across time, making them highly sensitive to changes in input data distribution [2]. This sensitivity can result in drastic changes to spiking behavior across the network, ultimately degrading performance when faced with distribution shifts. Understanding and enhancing the robustness of SNNs under such conditions is therefore a critical research direction.

In real-world applications, it is common that the distribution of the training data (*a.k.a.* source domain) and the test data (*a.k.a.* target domain) are different due to variations in lighting, background, sensor noise, or environmental conditions. This phenomenon, known as domain shift, can significantly degrade the performance of machine learning models [15, 25]. SNNs are particularly vulnerable to domain shifts, as even minor changes in input data can disrupt the temporal dynamics and spiking

behavior in intermediate layers, leading to poor generalization. Traditional test-time adaptation (TTA) solutions such as retraining or fine-tuning on target domain data with help of source data related proxy task [41], statistics of source data [33], or a batch of test data [42], are often impractical in real-world scenarios due to the unavailability of source data or other test samples, particularly in privacy-sensitive or resource-constrained environments. Source-free and single-instance TTA methods [9, 23, 47] offer a promising alternative by enabling the model to adapt to the target domain during inference without access to source data, which is typically defined (and also in this work) as one iteration of training adaptation with one test sample.

Among existing source-free and single-instance TTA methods, MEMO [47] and SITA [23] are two representative approaches, but both face fundamental limitations when applied to SNNs. MEMO optimizes the entropy of the averaged prediction across multiple augmented views of a test sample, enforcing output probability consistency. However, this strategy may not be optimal for SNNs. In SNNs, output probability distributions reflect only high-level semantic information and fail to capture the fine-grained spiking dynamics that encode essential features which prevents MEMO from effectively mitigating domain shifts within SNNs' internal representations. On the other hand, SITA adapts batch normalization (BN) statistics by shifting them toward those computed from test-time augmentations, but this approach is also unsuitable for SNNs. In SNNs, many models lack BN layers [27, 46], which limits the applicability of BN-based adaptation methods such as SITA in SNNs. Additionally, due to the sparsity of SNN activations, modifying BN statistics does not significantly alter neuronal spiking patterns, further reducing its ability to facilitate effective adaptation.

In this work, we propose a novel method names **SPike-Aware Consistency Enhancement (SPACE)**, which is the first source-free and single-instance TTA approach specifically designed for SNNs. SPACE performs adaptation using only a single test point without access to source data, making it particularly suitable for real-world scenarios where source data are unavailable or privacy-sensitive. By leveraging the inherent spike dynamics of SNNs, SPACE maximizes the consistency in spike-behavior-based local feature maps across augmented samples of the same input, ensuring robust and efficient adaptation in deep SNNs. Unlike existing TTA methods, which often overlook the unique characteristics of SNNs, SPACE directly exploits spike-based representations for adaptation. Our contributions can be summarized as follows

1. To the best of our knowledge, we are the first TTA method tailored for SNNs, which operates effectively using only a single test sample. This addresses the unique challenges of adapting SNNs in scenarios where source data are unavailable, while maintaining efficiency and scalability.
2. Our method introduces a consistency-driven optimization framework to enhance the similarity of spike-behavior-based local feature maps across augmented samples. By leveraging spike dynamics, this approach ensures robust adaptation in deep SNNs.
3. To assess the effectiveness and robustness of our proposed method, we perform extensive experiments across multiple benchmarks, including CIFAR-10, CIFAR-100 [26], Tiny-ImageNet, ImageNet [6], and the neuromorphic dataset DVS Gesture [1]. Furthermore, we validate the adaptability of our method across different model architectures, specifically testing on SNN-VGG [24, 40], SNN-ResNet11 [14, 27], Spike-driven Transformer V3 [44], and SNN-ConvLSTM [39]. The results demonstrate that our approach not only achieves consistent performance improvements across datasets but also generalizes well to different network structures, showcasing its broad applicability and robustness.

2 Related Work

2.1 SNN-based Deep Learning

Over the years, significant progress has been made in SNN-based deep learning. Many approaches primarily relied on converting pre-trained ANN models into SNNs, enabling SNNs to inherit the representational power of ANNs while benefiting from spike-based computations [3, 8, 19, 22]. However, such conversion methods often suffer from performance degradation due to differences in activation dynamics. To overcome this, direct training of SNNs using surrogate gradient methods has gained traction, enabling end-to-end optimization of spiking models [7, 11, 30, 32, 46]. Rathi et al. [34] proposed a hybrid method that combines conversion and surrogate gradient-based method, achieving

state-of-the-art performance. These advancements have not only solved the challenge owing to the non-differentiable nature of spike functions and the the inherent complexity of temporal dynamics, but also led to the development of sophisticated SNN architectures, such as spiking convolutional networks [27, 43] and spiking recurrent networks [45, 48], which have denoted promising results in tasks like image classification, speech recognition, and event-driven sensor data analysis.

A critical limitation of current SNN-based deep learning approaches is their poor robustness to testing-time variations. Unlike ANNs, which operate on continuous activations and can leverage well-established testing-time adaptation techniques, SNNs are highly sensitive to input perturbations due to their dependence on precise spike timing and temporal dynamics. According to our experimental results presented in section 4, existing SNN models, which are typically trained offline, lack mechanisms to dynamically adapt to changing environments or incoming data distributions at testing time. Addressing these shortcomings is essential for deploying SNNs in practical applications, particularly those requiring real-time adaptability.

2.2 Test-time Adaptation

Test-time adaptation (TTA) is a rapidly growing area in machine learning that tackles the challenge of adapting pre-trained models to unseen or shifted distributions during inference [21, 31, 41, 42]. Test-time training (TTT) [41] performs online updates to model parameters using supervised proxy task on the test data. However, the dependence on source data makes these methods impractical in scenarios where the source domain is unavailable during deployment due to privacy or storage constraints. To overcome source dependency, source-free TTA methods have been proposed, which perform adaptation using only test-time inputs. TENT [42] utilizes a straightforward yet effective entropy minimization approach to optimize batch normalization parameters during test time, without relying on any proxy task during training. Lee et al. [28] employs pseudo-labeling to adjust model predictions.

Although these approaches eliminate the need for source data, they often assume batch-level adaptation, relying on test-time statistics computed over multiple samples. This assumption limits their applicability in real-world settings where only single test points are available at a time. MEMO [47] addresses this scenario, proposing minimizing the marginal output distribution in the increases of the single test point. The objective in MEMO encourages the model to produce consistent predictions across different augmentations, thus enforcing the invariances encoded in these augmentations, while also maintaining confidence in its predictions. Another TTA method, SITA [23], adapts batch normalization statistics at inference by shifting them toward those computed from a batch of augmented versions of the single test instance.

MEMO has shown that enforcing consistency among augmented samples improves TTA performance. However, in deep SNNs, where information is transmitted through discrete spikes, backpropagation tied to output objectives suffers from temporal information loss, making effective TTA challenging. Moreover, MEMO fails to capture the domain shift-induced variations in the internal behavior of the SNN, such as changes in neuron activations and spike patterns, which are critical for robust adaptation in SNNs. Although SITA avoids backpropagation, it also struggles to accurately model the intrinsic temporal dynamics of SNNs, limiting its ability to align augmented samples effectively. To overcome these issues, we enforce consistency by directly aligning the spike patterns and behaviors of augmented samples within the SNN framework. Unlike BN-dependent methods like SITA, our approach works regardless of the presence of BN layers, ensuring broader compatibility with various SNN architectures.

3 Proposed Method

3.1 Preliminary

SNNs emulate biological neurons by transmitting and encoding information through discrete spikes. Among various neuron models, the Leaky Integrate-and-Fire (LIF) neuron [5] is widely adopted for its balance between biological realism and computational efficiency. Its membrane potential dynamics follow

$$\tau_m \frac{dU(t)}{dt} = -U(t) + RI(t), \tag{1}$$

where $U(t)$ represents the membrane potential of the neuron at time t , τ_m is the membrane time constant, R denotes the input resistance and $I(t)$ is the input current received from pre-synaptic neurons or inputs. When $U(t)$ exceeds a predefined threshold U_{th} , the neuron emits a spike and its membrane potential is reset to a resting value, typically 0 or $U(t) - U_{th}$. Following [11], Equation 1 is discretized as

$$u_i^t = (1 - \frac{1}{\tau_m})u_i^{t-1} + \frac{1}{\tau_m} \sum_j w_{ij}o_j^t. \quad (2)$$

Here, j is the index of pre-synaptic neurons, o_j is the binary spike activation, and w_{ij} stands for weight connections between pre- and post-neurons. Figure 1 illustrates the LIF neuron model, depicting membrane potential evolution and spike generation in response to input spikes [10].

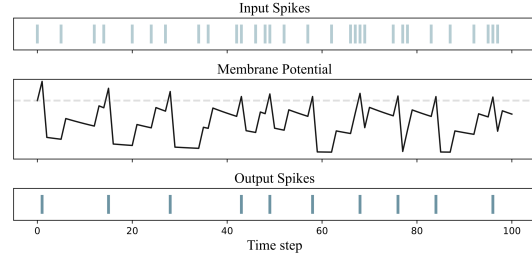


Figure 1: Illustration of spike and membrane potential dynamics in LIF neurons. When the membrane potential reaches the threshold, it is reset by subtracting the threshold value, triggering the neuron to fire a spike.

The spiking mechanism in SNNs introduces non-differentiability, making it difficult to apply standard gradient-based optimization methods for training or test-time adaptation. To address this, surrogate gradient methods approximate the non-differentiable spike function with a smooth surrogate during the backward pass. A simple approach is the shifted Heaviside step function, where the gradient of o_j , the spiking activation function of neuron j , with respect to U is defined as

$$\frac{\partial o_j}{\partial U} \triangleq \begin{cases} 1, & \text{if } U \geq U_{th}, \\ 0, & \text{if } U < U_{th}. \end{cases} \quad (3)$$

While this is not an exact solution, it is valid because a reset occurs after a spike is generated when $U \geq U_{th}$.

These foundational techniques for SNN training, including LIF dynamics and surrogate gradient approximations, form the basis for our proposed method, which focuses on enhancing TTA by ensuring consistency in spiking behavior across augmented samples.

3.2 Spike-Aware Consistency Enhancement

Algorithm Design Overview The proposed algorithm through spike-aware consistency enhancement (SPACE) for test-time adaptation is designed to improve test-time robustness of SNNs, as shown in Figure 2. We first generate an augmented batch from a single test sample using various augmentation techniques, introducing diversity while retaining the core characteristics of the original sample. This augmented batch is passed through the model to obtain local feature maps, represented by spike counts over time. Next, the model is adapted by maximizing the similarity across the feature maps of the augmented samples, promoting consistency in feature representations. Finally, the adapted model predicts the label of the original test sample, ensuring robust performance under test-time conditions. This approach enhances the model’s ability to generalize to unseen test samples, particularly in shifted domains. The overall method is presented in Algorithm 1, and the details are introduced below. The code will be made available after acceptance.

Spike-Aware Feature Maps SPACE aims to adapt pre-trained SNN-based models M_θ (with parameters $\theta \in \Theta$) during inference to improve performance under distribution shifts, without requiring ground truth labels or access to source data. No specific training process is required, nor do we impose particular constraints on the model. The only assumptions are that θ can be adjusted and that the model produces intermediate feature maps $\mathbf{F}(\mathbf{x})$, which is differentiable with respect to θ and can be utilized for further analysis and adaptation. Here, $\mathbf{x} \in \mathcal{X}$ is a single test point that is presented to M_θ . It is worth noting that this is a reasonable assumption, supported by a recent advance [36] that suggest gradient back-propagation can be implemented on spiking neuromorphic hardware. Aligned with previous work [23, 47], we achieve test-time robustness by leveraging data augmentations and a self-supervised adaptation objective. In our work, a set of augmentation functions with different

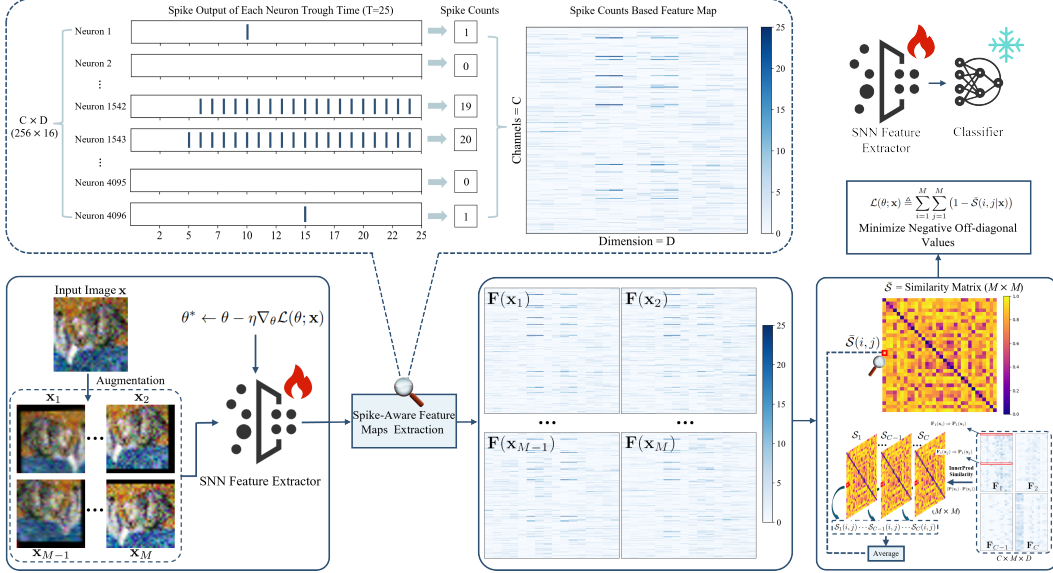


Figure 2: Overview of the **SPike-Aware Consistency Enhancement (SPACE)** framework for TTA in SNNs. The test sample is selected from CIFAR-10-C dataset [15] with Gaussian Noise corruption at level 5. The model here follows the VGG9 architecture. The process involves four main steps: 1) Generate an augmented batch from the single test sample. 2) Pass the augmented batch through the model to obtain local feature maps, represented by the spike counts over the processing time. 3) Adapt the model by maximizing the similarity across the local feature maps of the augmented samples. 4) Use the adapted model to predict the label of the original test sample.

intensities selected from $\mathcal{A} \triangleq \{a_1, \dots, a_N\}$ is applied to a single test input \mathbf{x} , forming an augmented batch of samples $\mathcal{B} = \{\mathbf{x}_1, \mathbf{x}_2, \dots, \mathbf{x}_M\}$, $M \leq N$. Using this batch, we align the spike dynamics extracted from augmentations, ensuring that the model produces reliable and robust predictions in the presence of distribution shifts.

Different from MEMO [47], which adapts the model during test time via the conditional output distribution $p_\theta(y|\mathbf{x})$ of the model’s last layer, SPACE leverages the dynamic behavior of intermediate layers in the SNN that plays a crucial role in determining the temporal information and semantic representation of the final output. SNNs encode information through temporal dynamics and spike sparsity. These behavioral characteristics are particularly prominent in the intermediate layers and can be represented by feature maps $\mathbf{F}(\mathbf{x})$. Unlike ANNs, these characteristics in SNNs cannot be fully captured by the output probability distribution alone. Another advantage of intermediate feature maps is its highly sensitivity to changes in the input distribution due to the event-driven nature of SNNs. When the input data undergoes a distribution shift, the spiking patterns in the intermediate layers may change significantly, thereby impacting the final output. Optimizing the consistency of spiking behavior in intermediate layers can effectively mitigate feature variations caused by distribution shifts, thereby enhancing the robustness of models.

To leverage the feature maps from the intermediate layers of the SNN, we focus on the spike activity over the entire time window. As described in subsection 3.1, each neuron j in an SNN can either fire a spike (outputting 1) or remain silent (outputting 0) at each time step t , represented by the binary function o_j^t . The temporal spike patterns of the network are captured in the feature map $\mathbf{O}(\mathbf{x}_i) \in \mathbb{R}^{T \times C \times H \times W}$, where T denotes the number of time steps, C represents the number of channels, and H and W are the spatial dimensions of the local feature maps. \mathbf{x}_i refers to the i -th sample in the augmented batch. Our primary objective is to use the total spike counts of the feature maps from either the last layer or the penultimate layer of the feature extraction network, depending on whether the final feature map is pooled into a 1×1 matrix. Let $\mathcal{F} = \{\mathbf{F}(\mathbf{x}_1), \mathbf{F}(\mathbf{x}_2), \dots, \mathbf{F}(\mathbf{x}_M)\}$ denote the collection of feature maps, where each $\mathbf{F}(\mathbf{x}_i) \in \mathbb{R}^{C \times D}$ represents the total spike counts of neurons across different channels, with $D = H \times W$ indicating the spatial dimensionality.

There are several reasons for choosing the total spike counts as the observation metric. First, SNNs typically operate over a time window ranging from 25 to thousands time steps [4, 13, 27, 34, 38],

Algorithm 1 SPACE for Test-Time Adaptation in SNNs

- 1: **Input:** Test sample \mathbf{x} , augmentation functions $\mathcal{A} = \{a_1, \dots, a_N\}$, model θ , learning rate η
 - 2: **Output:** Prediction y^* of \mathbf{x} using the updated model
 - 3: **Step 1: Generate augmented batch**
 - 4: Initialize $\mathcal{B} = \emptyset$
 - 5: **for** a_k in a subset $\{a_1, \dots, a_M\}$ of \mathcal{A} **do**
 - 6: $\mathbf{x}_k = a_k(\mathbf{x})$, add \mathbf{x}_k to \mathcal{B}
 - 7: **end for**
 - 8: **Step 2: Extract feature maps**
 - 9: Pass \mathcal{B} through SNN, obtain $\mathcal{F} = \{\mathbf{F}(\mathbf{x}_1), \dots, \mathbf{F}(\mathbf{x}_M)\}$
 - 10: **Step 3: Compute similarity**
 - 11: **for** each pair of $(\mathbf{F}(\mathbf{x}_i), \mathbf{F}(\mathbf{x}_j))$ in \mathcal{F} **do**
 - 12: Compute similarity $\bar{\mathcal{S}}(i, j|\mathbf{x})$ using Equation 4
 - 13: **end for**
 - 14: **Step 4: Update model parameters**
 - 15: Compute loss $\mathcal{L}(\theta; \mathbf{x})$ using Equation 5, update θ via SGD with η
 - 16: **Step 5: Predict**
 - 17: $y^* = \arg \max_y p_{\theta^*}(y|\mathbf{x})$
 - 18: **Return:** y^*
-

meaning that spike patterns across many time steps may be identical due to the repetitive nature of the spike dynamics. By comparing the cumulative spike counts instead of individual time-step patterns, we can effectively capture the temporal accumulation of spike activity while reducing redundancy. Second, the total spike counts reflects differences between augmented samples based on their overall spike dynamics, which is essential for our goal of aligning feature maps across augmentations. Finally, this representation significantly reduces the computational cost, as it condenses the temporal information into an aggregate value without requiring a step-by-step comparison of spike patterns.

Feature Maps Alignment The primary objective is to encourage the model to focus on invariant features that are crucial for classification, rather than being influenced by noise or minor transformations introduced by augmentations or distribution shifts in the training data. When the feature maps of augmented samples are highly similar, the model becomes less sensitive to variations at test time, thereby improving its ability to generalize to new, unseen, and unlabeled data. To measure the similarity between feature representations of the i -th and j -th samples, we employ channel-wise similarity between corresponding local feature vectors, $\mathbf{F}_c(\mathbf{x}_i)$ and $\mathbf{F}_c(\mathbf{x}_j)$. Here, $\mathbf{F}_c(\mathbf{x}_i)$ denotes the local feature vectors associated with channel c of the augmented sample \mathbf{x}_i . Specifically, we first normalize local feature vectors using a *softmax* function along the spatial dimensions, ensuring that the features are transformed into a probability distribution $\mathbf{P}_c(\mathbf{x}_i)$. This normalization highlights important spatial locations by amplifying prominent feature values and suppressing noise, enhancing feature distribution stability while enabling the subsequent similarity computation to capture both spatial and temporal characteristics effectively. To quantify the similarity between $\mathbf{F}(\mathbf{x}_i)$ and $\mathbf{F}(\mathbf{x}_j)$, we compute the average of channel-wise weighted inner product, defined as

$$\bar{\mathcal{S}}(i, j|\mathbf{x}) = \frac{1}{C} \sum_{c=1}^C \sum_{d=1}^D \mathbf{P}_{c,d}(\mathbf{x}_i) \cdot \mathbf{P}_{c,d}(\mathbf{x}_j), \quad (4)$$

The similarity measures the degree of overlap between the feature distributions, with higher values indicating greater consistency in spike-based representations across augmentations. Based on this similarity measure, we define the loss function for model adaptation given as

$$\mathcal{L}(\theta; \mathbf{x}) \triangleq \sum_{1 \leq j < i \leq M} (1 - \bar{\mathcal{S}}(i, j|\mathbf{x})). \quad (5)$$

Then, we adapt the model using stochastic gradient descent (SGD) for a single iteration with the learning rate η . By minimizing this loss function, we enforce consistency across the feature maps of different augmentations. This reduces the variability induced by augmentations, ensuring that the model learns stable and robust feature representations. Furthermore, by promoting feature consistency, this approach serves as a regularization mechanism, preventing over-fitting to specific augmentations and encouraging the model to focus on more fundamental and generalizable features.

While the proposed similarity measure effectively captures feature distribution overlap, we further investigated whether incorporating higher-dimensional feature relationships could enhance the consistency measure. Specifically, we experimented with a kernel embedding approach combined with Maximum Mean Discrepancy (MMD) in Appendix). However, this method did not yield noticeable performance improvements and introduced additional computational overhead, suggesting that the original similarity measure is already sufficient for our test-time adaptation.

Finally, we predict the classification via an updated model.

Discussion In SNNs, each local feature map captures distinct aspects of the input data and exhibits different spike patterns, both spatially and temporally. Since channels may have different active neurons, directly comparing the entire feature map fails to account for this variability. Instead, computing the similarity per channel and averaging the results focuses on the stability of feature representations within each channel. This isolates the contributions of active neurons, ensuring the similarity measure reflects meaningful changes rather than noise. It also minimizes the impact of irregular spike behavior or augmentation-induced noise in individual channels. Our experiments in subsection 4.2 show that directly comparing entire feature maps leads to ineffective TTA, reinforcing the importance of the per-channel similarity approach. Given that each channel learns distinct features, averaging the similarity within each channel provides a more reliable measure of feature map consistency, improving TTA performance.

4 Experimental Results

Datasets and Models The experiments were conducted on six benchmark datasets for out-of-distribution generalization: CIFAR-10-C, CIFAR-100-C, Tiny-ImageNet-C [15], ImageNet-V2 [35], ImageNet-R [17], and ImageNet-A [18]. The first three datasets include 15 corruption types across four categories and five severity levels, while the three ImageNet-based datasets capture real-world domain shifts, such as distributional discrepancies and semantic variations. Additionally, we evaluated on the neuromorphic dataset DVS Gesture-C [20], which introduces six corruption types. Four backbone models were used: 1) SNN-VGG with Batch-Normalization Through Time (BNTT)[24], using 25 inference steps; 2) SNN-ResNet with 30 inference steps[27]; 3) Spike-driven Transformer V3 [44], containing 19M parameters; and 4) SNN-ConvLSTM. All models were pre-trained on their respective source domains to ensure fair evaluation on datasets with domain shifts.

Compared Methods We compared our approach with models pre-trained on clean datasets and evaluated without any test-time adaptation (referred to as No Adapt). Additionally, since there are few TTA methods specifically designed for SNNs, we selected two representative traditional TTA methods, MEMO [47] and SITA [23], as baselines. These methods represent the current state-of-the-art for source-free and single-instance TTA, respectively. MEMO enforces output consistency among augmented samples, making it naturally compatible with SNNs by directly adjusting their final outputs. SITA, designed for models with BN layers, was adapted to SNN-VGG with BNTT by updating BN layer parameters during TTA.

Implementation details To maximize the effectiveness of our proposed method, all experiments conducted on CIFAR-10-C, CIFAR-100-C, Tiny-ImageNet-C, and DVS Gesture-C were performed with the highest severity level (level=5). In line with our setting and practical scenarios, the test batch size for all experiments was fixed to 1, and the model was updated only once per test sample. Following MEMO’s experimental setup, we applied AugMix [16] augmentation to generate diverse augmented samples, using a batch size of 32 for CIFAR-10-C, CIFAR-100-C, Tiny-ImageNet-C, and DVS Gesture-C, and 64 for the ImageNet series. Please refer to Appendix for more details.

4.1 Main Results

In this section, we compare the performance of the proposed SPACE method with two existing approaches: MEMO and SITA. To demonstrate the broad applicability of the proposed method, we evaluate all methods on CIFAR-10-C, CIFAR-100-C, and Tiny-ImageNet-C datasets using SNN-VGG, on CIFAR-10-C with SNN-ResNet11, on ImageNet series with Spike-driven Transformer V3, and on DVS Gesture-C with SNN-ConvLSTM, to demonstrate the broad applicability of our proposed method.

Table 1: Performance comparison on CIFAR-10-C, CIFAR-100-C, and Tiny-ImageNet-C with CNN-based SNN models regarding **Accuracy (%)**. The **bold** number indicates the best result.

| Method | Noise | | | Blur | | | | Weather | | | | Digital | | Average Acc. | | |
|----------------------------|--------------|--------------|--------------|--------------|--------------|--------------|--------------|--------------|--------------|--------------|--------------|--------------|--------------|--------------|--------------|--------------|
| | Gauss. | Shot | Impl. | Defoc. | Glass | Motion | Zoom | Snow | Fog | Frost | Brit. | Contr. | Elas. | | Pix. | JPEG |
| CIFAR-10-C, SNN-VGG9 | | | | | | | | | | | | | | | | |
| No Adapt | 72.38 | 74.70 | 58.57 | 63.05 | 63.96 | 64.44 | 71.33 | 76.32 | 43.57 | 75.72 | 82.44 | 22.54 | 75.01 | 70.25 | 84.28 | 66.57 |
| SITA | 73.06 | 74.15 | 58.41 | 62.94 | 64.21 | 64.36 | 70.72 | 76.67 | 43.40 | 75.24 | 82.51 | 22.02 | 74.74 | 69.62 | 84.16 | 66.41 |
| MEMO | 77.73 | 79.50 | 65.74 | 65.61 | 67.50 | 66.24 | 72.61 | 77.38 | 45.47 | 78.64 | 83.05 | 23.83 | 76.45 | 73.25 | 85.05 | 69.20 |
| SPACE (ours) | 77.98 | 79.34 | 69.41 | 71.59 | 67.76 | 72.14 | 74.67 | 78.43 | 52.80 | 79.59 | 83.22 | 23.85 | 75.49 | 76.24 | 82.88 | 71.03 |
| CIFAR-10-C, SNN-ResNet11 | | | | | | | | | | | | | | | | |
| No Adapt | 72.88 | 74.49 | 49.59 | 67.77 | 63.53 | 65.14 | 73.06 | 78.11 | 42.84 | 73.12 | 81.71 | 12.72 | 74.88 | 77.08 | 82.47 | 65.96 |
| MEMO | 74.21 | 75.50 | 51.35 | 68.11 | 64.65 | 65.37 | 73.96 | 78.32 | 43.47 | 73.39 | 81.82 | 13.63 | 75.54 | 77.54 | 83.24 | 66.67 |
| SPACE (ours) | 75.90 | 77.81 | 56.85 | 68.66 | 67.64 | 66.02 | 73.82 | 78.74 | 45.47 | 74.04 | 81.28 | 14.94 | 76.79 | 80.32 | 83.96 | 68.15 |
| CIFAR-100-C, SNN-VGG11 | | | | | | | | | | | | | | | | |
| No Adapt | 42.51 | 45.40 | 25.50 | 42.15 | 42.84 | 41.87 | 46.77 | 44.88 | 16.51 | 44.12 | 49.36 | 5.42 | 51.33 | 52.35 | 58.47 | 40.63 |
| SITA | 43.01 | 44.83 | 25.48 | 42.23 | 43.29 | 42.11 | 46.93 | 44.49 | 16.65 | 43.84 | 49.53 | 5.56 | 50.99 | 52.48 | 58.71 | 40.68 |
| MEMO | 43.46 | 45.41 | 26.07 | 42.47 | 43.90 | 42.55 | 47.21 | 44.74 | 16.76 | 44.34 | 49.95 | 5.62 | 51.24 | 52.82 | 59.29 | 41.06 |
| SPACE (ours) | 44.71 | 46.73 | 27.99 | 43.35 | 44.47 | 43.46 | 48.42 | 45.70 | 17.62 | 44.98 | 50.41 | 5.69 | 51.45 | 53.81 | 58.96 | 41.58 |
| Tiny-ImageNet-C, SNN-VGG11 | | | | | | | | | | | | | | | | |
| No Adapt | 12.43 | 15.20 | 8.74 | 7.58 | 6.50 | 14.48 | 13.59 | 15.58 | 5.27 | 18.06 | 15.01 | 1.32 | 20.53 | 31.62 | 31.15 | 14.47 |
| SITA | 12.71 | 15.17 | 8.87 | 7.56 | 6.57 | 14.57 | 13.94 | 15.72 | 5.32 | 18.05 | 14.82 | 1.38 | 21.45 | 32.20 | 31.51 | 14.66 |
| MEMO | 13.64 | 16.45 | 9.51 | 7.51 | 6.60 | 14.38 | 13.92 | 15.97 | 4.91 | 17.83 | 14.74 | 1.44 | 21.00 | 31.39 | 30.82 | 14.67 |
| SPACE (ours) | 16.71 | 19.44 | 11.72 | 9.62 | 7.31 | 16.57 | 15.61 | 18.66 | 6.01 | 21.02 | 17.53 | 1.51 | 21.96 | 31.89 | 31.63 | 16.48 |

Performance Comparison on CNN-based SNN Models

The results on CIFAR-10-C, CIFAR-100-C, and Tiny-ImageNet-C at level 5 corruption, shown in Table 1, highlight the effectiveness of SPACE. Key observations include the following: 1) **Superior Performance Across Methods:** SPACE consistently outperforms No Adapt, SITA, and MEMO in average accuracy across all datasets under both VGG and ResNet architectures. 2) **Broad Applicability:** SPACE demonstrates effectiveness across different CNN structures, showcasing its generalizability. 3) **Robustness on Complex Datasets:** A particularly notable result is SPACE’s performance on Tiny-ImageNet-C, where it surpasses all methods across every corruption type. This highlights its robustness in handling complex datasets like Tiny-ImageNet-C. 4) **Limitations of SITA on SNNs:** The SNN-ResNet does not include BN layers, rendering SITA inapplicable. Furthermore, SITA performs worse than No Adapt, indicating its ineffectiveness for SNNs. This may be attributed to the spike-based transmission in SNNs: directly adjusting BN parameters without gradient guidance can disrupt spike information, leading to significant performance degradation. 5) **Comparison with MEMO:** While SPACE generally outperforms MEMO and SITA, MEMO exhibits slightly better performance in a few specific cases, such as JPEG corruption on CIFAR-10-C (85.05% for MEMO vs. 82.88% for SPACE) and CIFAR-100-C (59.29% for MEMO vs. 58.96% for SPACE). These minor differences suggest MEMO may have an advantage under certain corruption types, but they do not detract from SPACE’s overall superiority.

Table 2: Performance comparison on ImageNet-V2/R/A with Spike-driven Transformer V3 regarding **Accuracy (%)**. The **bold** number indicates the best result.

| Method | Accuracy (%) | | | |
|--------------|--------------|--------------|--------------|--------------|
| | V2 | R | A | Avg. |
| No Adapt | 67.64 | 41.94 | 15.12 | 41.57 |
| MEMO | 67.57 | 42.15 | 14.97 | 41.56 |
| SPACE (ours) | 68.82 | 45.07 | 16.22 | 43.37 |

Performance Comparison on Spike-driven Transformer V3

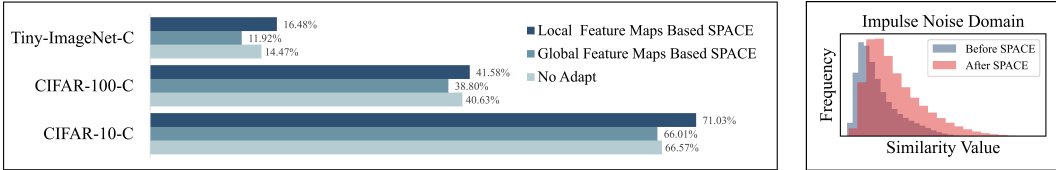
To explore the real-world impact of SPACE, we conducted tests on diverse datasets, including ImageNet-V2, ImageNet-R, and ImageNet-A. Furthermore, to evaluate its adaptability in deeper SNN architectures, we tested SPACE on the state-of-the-art Spike-Event Transformer V3. As shown in Table 2, SPACE consistently outperforms MEMO, achieving a 1.80% improvement, which demonstrates its robustness in real-world scenarios and its effectiveness in advanced SNN models.

Performance Comparison on ConvLSTM-based SNN Model

SNNs are inherently well-suited for processing event-based neuromorphic data, thanks to their temporal dynamics and energy efficiency. The DVS-Gesture dataset [1] provides an ideal benchmark to evaluate the performance of SPACE on neuromorphic datasets, highlighting its compatibility with dynamic vision tasks and data with temporal structures. To further explore potential network architectures, we incorporated ConvLSTM. As shown in Table 3, our approach achieves significantly better results compared to existing methods, demonstrating its effectiveness and adaptability.

Table 3: Performance comparison on DVS Gesture-C with ConvLSTM-based SNN model regarding **Accuracy (%)**. The **bold** number indicates the best result.

| Method | Accuracy (%) | | | | | | Avg. |
|--------------|--------------|--------------|------------------|--------------|---------------|--------------|--------------|
| | DropPixel | DropEvent | RefractoryPeriod | TimeJitter | SpatialJitter | UniformNoise | |
| No Adapt | 53.03 | 54.55 | 36.74 | 31.06 | 92.05 | 91.67 | 59.85 |
| MEMO | 56.06 | 55.30 | 36.74 | 30.68 | 90.91 | 91.67 | 60.23 |
| SPACE (ours) | 57.20 | 57.95 | 52.27 | 43.18 | 92.42 | 92.42 | 65.91 |



(a) Local feature maps based SPACE outperforms global feature maps based SPACE. (b) Similarity distribution of spike count feature maps before and after SPACE adaptation.

Figure 3: Results of ablation study.

4.2 Ablation Studies

Local vs. Global Feature Map Similarity We compared the performance of local versus global feature map similarity for our proposed method. The results in Figure 3a clearly illustrate the advantage of using similarity of local feature maps over global feature maps. While the global approach does not account for variability in neuron activations across channels, the local method isolates the contributions of active neurons within each channel, offering a more stable and meaningful measure of feature map consistency. As shown in Figure 3a, the local method yields a substantial accuracy improvement, whereas the global approach negatively impacts performance across all three datasets. This demonstrates that emphasizing individual channel stability leads to better generalization and adaptation. These findings underscore the distinct roles of each channel in SNNs and highlight the limitations of comparing entire feature maps.

Effect of SPACE on Feature Map Similarity To further investigate the impact of SPACE adaptation on the feature map similarity, we analyzed the distribution of similarity values (computed using Equation 4) across the CIFAR-10-C dataset. As shown in Figure 3b, we observe a noticeable increase in the similarity between the original samples and their augmented counterparts after applying SPACE adaptation, particularly in the Impulse Noise domain. The similarity distributions between spike counts based feature maps in these domains indicate that the feature map consistency improves following the adaptation process. Specifically, the "After SPACE Adaptation" distributions shift towards higher similarity values, reflecting the enhanced alignment of feature maps across augmented samples. This demonstrates the effectiveness of SPACE adaptation in increasing the stability of feature representations and improving generalization under various augmentation conditions.

5 Conclusion and Limitation

In this work, we propose SPike-Aware Consistency Enhancement (SPACE), the first source-free and single-instance TTA method tailored for SNNs. By leveraging the unique spike-driven dynamics of SNNs, SPACE optimizes spike-behavior-based feature map consistency across augmented samples, addressing the limitations of ANN-based TTA methods that overlook the temporal and sparse nature of SNN computations. Experiments on CIFAR-10, CIFAR-100, Tiny-ImageNet, ImageNet, and DVS Gesture series datasets show that SPACE consistently improves performance under severe corruptions and generalizes well across architectures, demonstrating robustness to domain shifts. However, SPACE's reliance on backpropagation may limit its applicability in resource-constrained scenarios. Future work will explore alternative optimization strategies to expand its practicality for neuromorphic hardware and energy-efficient AI.

References

- [1] Arnon Amir, Brian Taba, David Berg, Timothy Melano, Jeffrey McKinstry, Carmelo Di Nolfo, Tapan Nayak, Alexander Andreopoulos, Guillaume Garreau, Marcela Mendoza, et al. A low power, fully event-based gesture recognition system. In *Proceedings of the IEEE conference on computer vision and pattern recognition*, pages 7243–7252, 2017.
- [2] Guillaume Bellec, Franz Scherr, Anand Subramoney, Elias Hajek, Darjan Salaj, Robert Legenstein, and Wolfgang Maass. A solution to the learning dilemma for recurrent networks of spiking neurons. *Nature communications*, 11(1):3625, 2020.
- [3] Tong Bu, Wei Fang, Jianhao Ding, PENGLIN DAI, Zhaofei Yu, and Tiejun Huang. Optimal ANN-SNN conversion for high-accuracy and ultra-low-latency spiking neural networks. In *International Conference on Learning Representations*, 2022. URL https://openreview.net/forum?id=7B3IJMM1k_M.
- [4] Yongqiang Cao, Yang Chen, and Deepak Khosla. Spiking deep convolutional neural networks for energy-efficient object recognition. *International Journal of Computer Vision*, 113:54–66, 2015.
- [5] Peter Dayan and Laurence F Abbott. *Theoretical neuroscience: computational and mathematical modeling of neural systems*. MIT press, 2005.
- [6] Jia Deng, Wei Dong, Richard Socher, Li-Jia Li, Kai Li, and Li Fei-Fei. Imagenet: A large-scale hierarchical image database. In *2009 IEEE conference on computer vision and pattern recognition*, pages 248–255. Ieee, 2009.
- [7] Shikuang Deng, Hao Lin, Yuhang Li, and Shi Gu. Surrogate module learning: Reduce the gradient error accumulation in training spiking neural networks. In *International Conference on Machine Learning*, pages 7645–7657. PMLR, 2023.
- [8] Jianhao Ding, Zhaofei Yu, Yonghong Tian, and Tiejun Huang. Optimal ann-snn conversion for fast and accurate inference in deep spiking neural networks. In Zhi-Hua Zhou, editor, *Proceedings of the Thirtieth International Joint Conference on Artificial Intelligence, IJCAI-21*, pages 2328–2336. International Joint Conferences on Artificial Intelligence Organization, 8 2021. doi: 10.24963/ijcai.2021/321. URL <https://doi.org/10.24963/ijcai.2021/321>. Main Track.
- [9] Haoyu Dong, Nicholas Konz, Hanxue Gu, and Maciej A Mazurowski. Medical image segmentation with intent: Integrated entropy weighting for single image test-time adaptation. In *Proceedings of the IEEE/CVF Conference on Computer Vision and Pattern Recognition*, pages 5046–5055, 2024.
- [10] Jason K Eshraghian, Max Ward, Emre O Neftci, Xinxin Wang, Gregor Lenz, Girish Dwivedi, Mohammed Bannamoun, Doo Seok Jeong, and Wei D Lu. Training spiking neural networks using lessons from deep learning. *Proceedings of the IEEE*, 2023.
- [11] Wei Fang, Zhaofei Yu, Yanqi Chen, Timothée Masquelier, Tiejun Huang, and Yonghong Tian. Incorporating learnable membrane time constant to enhance learning of spiking neural networks. In *Proceedings of the IEEE/CVF international conference on computer vision*, pages 2661–2671, 2021.
- [12] Samanwoy Ghosh-Dastidar and Hojjat Adeli. Spiking neural networks. *International journal of neural systems*, 19(04):295–308, 2009.
- [13] Bing Han, Gopalakrishnan Srinivasan, and Kaushik Roy. Rmp-snn: Residual membrane potential neuron for enabling deeper high-accuracy and low-latency spiking neural network. In *Proceedings of the IEEE/CVF conference on computer vision and pattern recognition*, pages 13558–13567, 2020.
- [14] Kaiming He, Xiangyu Zhang, Shaoqing Ren, and Jian Sun. Deep residual learning for image recognition. In *Proceedings of the IEEE conference on computer vision and pattern recognition*, pages 770–778, 2016.
- [15] Dan Hendrycks and Thomas Dietterich. Benchmarking neural network robustness to common corruptions and perturbations. *Proceedings of the International Conference on Learning Representations*, 2019.
- [16] Dan Hendrycks, Norman Mu, Ekin D. Cubuk, Barret Zoph, Justin Gilmer, and Balaji Lakshminarayanan. AugMix: A simple data processing method to improve robustness and uncertainty. *Proceedings of the International Conference on Learning Representations (ICLR)*, 2020.
- [17] Dan Hendrycks, Steven Basart, Norman Mu, Saurav Kadavath, Frank Wang, Evan Dorundo, Rahul Desai, Tyler Zhu, Samyak Parajuli, Mike Guo, et al. The many faces of robustness: A critical analysis of out-of-distribution generalization. In *Proceedings of the IEEE/CVF international conference on computer vision*, pages 8340–8349, 2021.

- [18] Dan Hendrycks, Kevin Zhao, Steven Basart, Jacob Steinhardt, and Dawn Song. Natural adversarial examples. *CVPR*, 2021.
- [19] Yangfan Hu, Qian Zheng, Xudong Jiang, and Gang Pan. Fast-snn: fast spiking neural network by converting quantized ann. *IEEE Transactions on Pattern Analysis and Machine Intelligence*, 2023.
- [20] Yifan Huang, Wei Fang, Zhengyu Ma, Guoqi Li, and Yonghong Tian. Flexible and scalable deep dendritic spiking neural networks with multiple nonlinear branching. *arXiv preprint arXiv:2412.06355*, 2024.
- [21] Yusuke Iwasawa and Yutaka Matsuo. Test-time classifier adjustment module for model-agnostic domain generalization. *Advances in Neural Information Processing Systems*, 34:2427–2440, 2021.
- [22] Haiyan Jiang, Srinivas Anumasa, Giulia De Masi, Huan Xiong, and Bin Gu. A unified optimization framework of ANN-SNN conversion: Towards optimal mapping from activation values to firing rates. In Andreas Krause, Emma Brunskill, Kyunghyun Cho, Barbara Engelhardt, Sivan Sabato, and Jonathan Scarlett, editors, *Proceedings of the 40th International Conference on Machine Learning*, volume 202 of *Proceedings of Machine Learning Research*, pages 14945–14974. PMLR, 23–29 Jul 2023. URL <https://proceedings.mlr.press/v202/jiang23a.html>.
- [23] Ansh Khurana, Sujoy Paul, Piyush Rai, Soma Biswas, and Gaurav Aggarwal. Sita: Single image test-time adaptation. *arXiv preprint arXiv:2112.02355*, 2021.
- [24] Youngeun Kim and Priyadarshini Panda. Revisiting batch normalization for training low-latency deep spiking neural networks from scratch. *Frontiers in neuroscience*, 15:773954, 2021.
- [25] Pang Wei Koh, Shiori Sagawa, Henrik Marklund, Sang Michael Xie, Marvin Zhang, Akshay Balsubramani, Weihua Hu, Michihiro Yasunaga, Richard Lanus Phillips, Irena Gao, et al. Wilds: A benchmark of in-the-wild distribution shifts. In *International conference on machine learning*, pages 5637–5664. PMLR, 2021.
- [26] A Krizhevsky. Learning multiple layers of features from tiny images. *Master’s thesis, University of Tront*, 2009.
- [27] Chankyu Lee, Syed Shakib Sarwar, Priyadarshini Panda, Gopalakrishnan Srinivasan, and Kaushik Roy. Enabling spike-based backpropagation for training deep neural network architectures. *Frontiers in neuroscience*, 14:497482, 2020.
- [28] Dong-Hyun Lee et al. Pseudo-label: The simple and efficient semi-supervised learning method for deep neural networks. In *Workshop on challenges in representation learning, ICML*, volume 3, page 896. Atlanta, 2013.
- [29] Gregor Lenz, Kenneth Chaney, Sumit Bam Shrestha, Omar Oubari, Serge Picaud, and Guido Zarrella. Tonic: event-based datasets and transformations., July 2021. URL <https://doi.org/10.5281/zenodo.5079802>. Documentation available under <https://tonic.readthedocs.io>.
- [30] Shuang Lian, Jiangrong Shen, Qianhui Liu, Ziming Wang, Rui Yan, and Huajin Tang. Learnable surrogate gradient for direct training spiking neural networks. In *IJCAI*, pages 3002–3010, 2023.
- [31] Jian Liang, Dapeng Hu, and Jiashi Feng. Do we really need to access the source data? source hypothesis transfer for unsupervised domain adaptation. In *International conference on machine learning*, pages 6028–6039. PMLR, 2020.
- [32] Emre O Neftci, Hesham Mostafa, and Friedemann Zenke. Surrogate gradient learning in spiking neural networks: Bringing the power of gradient-based optimization to spiking neural networks. *IEEE Signal Processing Magazine*, 36(6):51–63, 2019.
- [33] Shuaicheng Niu, Chunyan Miao, Guohao Chen, Pengcheng Wu, and Peilin Zhao. Test-time model adaptation with only forward passes. *arXiv preprint arXiv:2404.01650*, 2024.
- [34] Nitin Rathi, Gopalakrishnan Srinivasan, Priyadarshini Panda, and Kaushik Roy. Enabling deep spiking neural networks with hybrid conversion and spike timing dependent backpropagation. In *International Conference on Learning Representations*, 2020. URL <https://openreview.net/forum?id=B1xSperKvH>.
- [35] Benjamin Recht, Rebecca Roelofs, Ludwig Schmidt, and Vaishaal Shankar. Do imagenet classifiers generalize to imagenet? In *International conference on machine learning*, pages 5389–5400. PMLR, 2019.
- [36] Alpha Renner, Forrest Sheldon, Anatoly Zlotnik, Louis Tao, and Andrew Sornborger. The backpropagation algorithm implemented on spiking neuromorphic hardware. *Nature Communications*, 15(1):9691, 2024.

- [37] Kaushik Roy, Akhilesh Jaiswal, and Priyadarshini Panda. Towards spike-based machine intelligence with neuromorphic computing. *Nature*, 575(7784):607–617, 2019.
- [38] Abhronil Sengupta, Yuting Ye, Robert Wang, Chiao Liu, and Kaushik Roy. Going deeper in spiking neural networks: Vgg and residual architectures. *Frontiers in neuroscience*, 13:95, 2019.
- [39] Xingjian Shi, Zhourong Chen, Hao Wang, Dit-Yan Yeung, Wai-Kin Wong, and Wang-chun Woo. Convolutional lstm network: A machine learning approach for precipitation nowcasting. *Advances in neural information processing systems*, 28, 2015.
- [40] Karen Simonyan and Andrew Zisserman. Very deep convolutional networks for large-scale image recognition. *arXiv preprint arXiv:1409.1556*, 2014.
- [41] Yu Sun, Xiaolong Wang, Zhuang Liu, John Miller, Alexei Efros, and Moritz Hardt. Test-time training with self-supervision for generalization under distribution shifts. In *International conference on machine learning*, pages 9229–9248. PMLR, 2020.
- [42] Dequan Wang, Evan Shelhamer, Shaoteng Liu, Bruno Olshausen, and Trevor Darrell. Tent: Fully test-time adaptation by entropy minimization. *arXiv preprint arXiv:2006.10726*, 2020.
- [43] Yujie Wu, Lei Deng, Guoqi Li, Jun Zhu, and Luping Shi. Spatio-temporal backpropagation for training high-performance spiking neural networks. *Frontiers in neuroscience*, 12:331, 2018.
- [44] Man Yao, Xuerui Qiu, Tianxiang Hu, Jiakui Hu, Yuhong Chou, Keyu Tian, Jianxing Liao, Luziwei Leng, Bo Xu, and Guoqi Li. Scaling spike-driven transformer with efficient spike firing approximation training. *IEEE Transactions on Pattern Analysis and Machine Intelligence*, 2025.
- [45] Bojian Yin, Federico Corradi, and Sander M Bohté. Accurate and efficient time-domain classification with adaptive spiking recurrent neural networks. *Nature Machine Intelligence*, 3(10):905–913, 2021.
- [46] Friedemann Zenke and Surya Ganguli. Superspike: Supervised learning in multilayer spiking neural networks. *Neural computation*, 30(6):1514–1541, 2018.
- [47] Marvin Zhang, Sergey Levine, and Chelsea Finn. Memo: Test time robustness via adaptation and augmentation. *Advances in neural information processing systems*, 35:38629–38642, 2022.
- [48] Hanle Zheng, Zhong Zheng, Rui Hu, Bo Xiao, Yujie Wu, Fangwen Yu, Xue Liu, Guoqi Li, and Lei Deng. Temporal dendritic heterogeneity incorporated with spiking neural networks for learning multi-timescale dynamics. *Nature Communications*, 15(1):277, 2024.

A Kernel-Based Consistency Regularization

To investigate whether higher-dimensional feature relationships can enhance the consistency measure, we integrate kernel embeddings into the loss function. The channel-wise feature probability distribution $\mathbf{P}_c(\mathbf{x}_i)$ can be mapped into a higher-dimensional reproducing kernel Hilbert space (RKHS) \mathcal{H} , using a Gaussian kernel defined as

$$k(\mathbf{z}, \mathbf{z}') = \exp\left(-\frac{\|\mathbf{z} - \mathbf{z}'\|^2}{2\sigma^2}\right), \quad (6)$$

where σ is the kernel bandwidth. The kernel function $k(\mathbf{z}, \mathbf{z}')$ implicitly defines a mapping $\phi: \mathcal{Z} \rightarrow \mathcal{H}$, such that the inner product in \mathcal{H} is given by the kernel:

$$k(\mathbf{z}, \mathbf{z}') = \langle \phi(\mathbf{z}), \phi(\mathbf{z}') \rangle_{\mathcal{H}}. \quad (7)$$

This allows us to compute relationships between feature vectors in a high-dimensional space without explicitly constructing $\phi(\cdot)$. To align feature distributions from augmented samples, we use the Mean Embedding of Distributions, which maps $\mathbf{P}_c(\mathbf{x}_i)$ into a single point $\mu_{\mathbf{P}_c(\mathbf{x}_i)}$ in RKHS. Specifically, the mean embedding is defined as

$$\mu_{\mathbf{P}_c(\mathbf{x}_i)} = \mathbb{E}_{\mathbf{z}_i \sim \mathbf{P}_c(\mathbf{x}_i)}[\phi(\mathbf{z}_i)]. \quad (8)$$

Given samples $\mathbf{z}_i \sim \mathbf{P}_c(\mathbf{x}_i)$, the embedding can be approximated as

$$\mu_{\mathbf{P}_c(\mathbf{x}_i)} \triangleq \frac{1}{D} \sum_{d=1}^D \phi(\mathbf{z}_{i_d}). \quad (9)$$

To measure the discrepancy between distributions $\mathbf{P}_c(\mathbf{x}_i)$ and $\mathbf{P}_c(\mathbf{x}_j)$ in RKHS, we employ the Maximum Mean Discrepancy (MMD):

$$\text{MMD}^2(\mathbf{P}_c(\mathbf{x}_i), \mathbf{P}_c(\mathbf{x}_j)) = \|\mu_{\mathbf{P}_c(\mathbf{x}_i)} - \mu_{\mathbf{P}_c(\mathbf{x}_j)}\|_{\mathcal{H}}^2. \quad (10)$$

Using the kernel trick, this can be computed without explicitly constructing $\phi(\cdot)$:

$$\text{MMD}^2(\mathbf{P}_c(\mathbf{x}_i), \mathbf{P}_c(\mathbf{x}_j)) = \frac{1}{D^2} \left\| \sum_{d=1}^D \phi(\mathbf{z}_{i_d}) - \sum_{d=1}^D \phi(\mathbf{z}_{j_d}) \right\|_{\mathcal{H}}^2. \quad (11)$$

Then we average the MMD values across all channels:

$$\text{MMD}^2(i, j | \mathbf{x}) = \frac{1}{C} \sum_{c=1}^C \text{MMD}^2(\mathbf{P}_c(\mathbf{x}_i), \mathbf{P}_c(\mathbf{x}_j)). \quad (12)$$

Finally, we integrate the average MMD values into the original loss function \mathcal{L} :

$$\mathcal{L}^*(\theta; \mathbf{x}) \triangleq \mathcal{L} + \lambda_{\text{MMD}} \sum_{1 \leq j < i \leq M} \text{MMD}^2(i, j | \mathbf{x}) \quad (13)$$

To evaluate the impact of incorporating kernel embedding into the loss function, we tested its performance on CIFAR-10-C dataset, using SNN-VGG9 model, as shown in Table 4. The results indicate that adding kernel embedding provides little to no improvement over the original SPACE method, with the average performance remaining nearly identical. This limited effectiveness can be attributed to several factors. First, the distribution differences introduced by augmentations, such as noise, blur, and weather effects, are relatively small, reducing the need for advanced alignment mechanisms like kernel embedding. Additionally, the existing similarity measures in SPACE already effectively capture the relationships between augmented samples, leaving little room for further optimization. Moreover, the added computational complexity of kernel embedding, especially the cost of kernel calculations, may even slightly hinder performance in scenarios where the original approach is already sufficient. These factors combined suggest that kernel embedding is not particularly beneficial in this experimental setting.

Table 4: Performance comparison of SPACE without/with kernel embedding (*k.e.*) on CIFAR-10-C with SNN-VGG9 model regarding **Accuracy (%)**. The **bold** number indicates the best result.

| Method | Noise | | | Blur | | | | Weather | | | | Digital | | | Average Acc. | |
|---------------------|--------------|--------------|--------------|--------------|--------------|--------------|--------------|--------------|--------------|--------------|--------------|--------------|--------------|--------------|--------------|--------------|
| | Gauss. | Shot | Impl. | Defoc. | Glass | Motion | Zoom | Snow | Fog | Frost | Brit. | Contr. | Elas. | Pix. | | JPEG |
| No Adapt | 72.38 | 74.70 | 58.57 | 63.05 | 63.96 | 64.44 | 71.33 | 76.32 | 43.57 | 75.72 | 82.44 | 22.54 | 75.01 | 70.25 | 84.28 | 66.57 |
| SPACE | 77.98 | 79.34 | 69.41 | 71.59 | 67.76 | 72.14 | 74.67 | 78.43 | 52.80 | 79.59 | 83.22 | 23.85 | 75.49 | 76.24 | 82.88 | 71.03 |
| SPACE + <i>k.e.</i> | 77.85 | 79.34 | 69.25 | 71.42 | 67.64 | 72.21 | 74.61 | 78.48 | 52.46 | 79.66 | 83.25 | 23.40 | 75.42 | 76.13 | 82.98 | 70.94 |

Table 5: Performance comparison of SPACE with different objectives on CIFAR-10-C with SNN-VGG9 model regarding **Accuracy (%)**. The **bold** number indicates the best result. Average membrane potential and spike through all time steps are referred as *a.m.p.* and *s.t.t.* respectively.

| Method | Noise | | | Blur | | | | Weather | | | | Digital | | | Average Acc. | |
|-----------------------|--------------|--------------|--------------|--------------|--------------|--------------|--------------|--------------|--------------|--------------|--------------|--------------|--------------|--------------|--------------|--------------|
| | Gauss. | Shot | Impl. | Defoc. | Glass | Motion | Zoom | Snow | Fog | Frost | Brit. | Contr. | Elas. | Pix. | | JPEG |
| No Adapt | 72.38 | 74.70 | 58.57 | 63.05 | 63.96 | 64.44 | 71.33 | 76.32 | 43.57 | 75.72 | 82.44 | 22.54 | 75.01 | 70.25 | 84.28 | 66.57 |
| SPACE | 77.98 | 79.34 | 69.41 | 71.59 | 67.76 | 72.14 | 74.67 | 78.43 | 52.80 | 79.59 | 83.22 | 23.85 | 75.49 | 76.24 | 82.88 | 71.03 |
| SPACE + <i>a.m.p.</i> | 74.87 | 76.05 | 61.64 | 64.90 | 65.79 | 65.88 | 72.22 | 77.66 | 45.66 | 76.64 | 82.81 | 21.57 | 75.53 | 70.91 | 84.74 | 67.79 |
| SPACE + <i>s.t.t.</i> | 72.74 | 73.84 | 57.86 | 62.91 | 63.66 | 64.33 | 70.94 | 76.35 | 43.16 | 74.77 | 82.30 | 21.20 | 74.24 | 69.35 | 83.97 | 66.11 |

B Exploration of Alternative Alignment Objectives

B.1 Two Alternative Alignment Objectives

Average Membrane Potential (SPACE + *a.m.p.*) In the main paper, we use feature maps based on the spike counts over the entire time window as the alignment objective. In this section, we explore an alternative biologically inspired metric: the average membrane potential obtained from the LIF neurons in the final layer of the feature extractor. Specifically, for a given test point \mathbf{x}_i , the membrane potentials are captured in the feature map $\mathbf{U}(\mathbf{x}_i) \in \mathbb{R}^{T \times C \times D}$, where T , C , and D represent the time steps, the number of channels, and the spatial dimensions, respectively. For LIF neurons that spike at a specific time step, we use the membrane potential after the LIF reset, which indirectly captures the spiking information. To obtain the primary objective feature map $\mathbf{F}(\mathbf{x}_i)$, we compute the temporal average of $\mathbf{U}(\mathbf{x}_i)$ along the first dimension. The resulting feature map is then used to calculate the loss following Equations 4 and Equation 5 in the main paper. Finally, the model is updated via SGD.

Spikes through All Time Steps (SPACE + *s.t.t.*) Instead of summing the spike counts over the temporal dimension, we explicitly retain the temporal information, resulting in a feature map with an additional dimension that captures the spiking activity at each time step. This approach preserves the precise temporal dynamics of the spikes and leverages them directly for alignment. Specifically, we align the channel-wise spiking activity across all time steps between each pair of augmented samples. The update rules remain consistent with those described in the main paper.

B.2 Experimental Results and Analysis

We implement the two approaches above and evaluate on CIFAR-10-C dataset with SNN-VGG9 model. The results are shown in Table 5.

Compared to No Adapt, SPACE + *a.m.p.* improves the generalization ability of the model. However, its performance is noticeably inferior to SPACE on the majority of corruptions. This may be due to the fact that the membrane potentials of the same sample under different augmentations tend to exhibit similar patterns, making them less effective in capturing the temporal distribution characteristics of SNNs. For example, in extreme cases where the membrane potential of a LIF neuron stays near the firing threshold throughout all time steps without crossing it, SPACE + *a.m.p.* fails to capture this information. In contrast, SPACE can reflect this behavior through spike counts, which more directly encode spiking activity.

SPACE + *s.t.t.* fails to improve the generalization ability of the model. We hypothesize that this is due to the model overfitting during the alignment process. Specifically, the updates made to minimize the alignment loss may inadvertently lead to excessive specialization to the augmented samples, thereby hindering its ability to generalize effectively to unseen corruptions.

C Additional Ablation Study

Effect of Augmentation Quantity per Test Point In the main paper, we follow MEMO [47] to determine the number of augmentations M . To analyze the effect of M on our method, we evaluated the average accuracy and the evaluation time per test point the same computing resource conditions on CIFAR-10-C using SNN-VGG9 with varying augmentation quantities $M = \{2, 4, 8, 16, 32, 64, 128\}$. As shown in Table 6, at least 8 augmentations are required to achieve noticeable performance improvement. For $M = \{32, 64, 128\}$, while the performance continues to improve gradually, the evaluation time increases significantly. Considering the trade-off between accuracy and evaluation time, $M = 32$ is the optimal choice.

Table 6: Performance comparison of SPACE with different augmentation quantities on CIFAR-10-C with SNN-VGG9 model regarding **Accuracy (%)** and **Evaluation Time** (seconds) per test point.

| | No Adapt | Number of Augmentation | | | | | | |
|-----------------|----------|------------------------|-------|-------|-------|-------|-------|-------|
| | | 2 | 4 | 8 | 16 | 32 | 64 | 128 |
| Accuracy | 66.57 | 54.60 | 66.91 | 69.77 | 70.60 | 71.03 | 71.07 | 71.11 |
| Evaluation Time | 0.144 | 0.318 | 0.320 | 0.327 | 0.339 | 0.345 | 0.443 | 0.788 |

D Additional Experimental Information

D.1 More Details on Datasets

In this paper, we conducted six static datasets and one neuromorphic dataset to evaluate the out-of-distribution generalization ability. They are CIFAR-10-C, CIFAR-100-C, Tiny-ImageNet-C [15], ImageNet-V2 [35], ImageNet-R [17], ImageNet-A [18] and DVS Gesture-C [20].

CIFAR-10-C, CIFAR-100-C, and Tiny-ImageNet-C These three datasets are commonly used benchmarks for evaluating the robustness of models under various types of input corruptions. They are derived from the original CIFAR-10, CIFAR-100, and Tiny-ImageNet datasets by applying 15 corruption types (*e.g.*, noise, blur, weather, and digital distortions) at 5 severity levels to the original CIFAR-10, CIFAR-100 [26], and Tiny-ImageNet [6] datasets, respectively. CIFAR-10-C and CIFAR-100-C consist of 10 and 100 classes, each with 50,000 training images and 10,000 testing images. Tiny-ImageNet-C, derived from Tiny-ImageNet, includes 200 classes with 100,000 training images and 10,000 validation images.

ImageNet V2/R/A ImageNet-V2, ImageNet-R, and ImageNet-A are three datasets designed to evaluate model robustness under different real-world challenges. ImageNet-V2 consists of a new set of images collected under similar conditions as the original ImageNet [6], serving as a test of distribution shift. ImageNet-R focuses on image classification robustness across various artistic renditions, such as paintings, sketches, and cartoons, covering 200 ImageNet classes. ImageNet-A, on the other hand, is an adversarially filtered subset of natural images that models often misclassify, targeting their inherent weaknesses. Compared to corruption-based datasets, these benchmarks provide a better reflection of real-world scenarios and challenges.

DVS Gesture-C DVS Gesture-C is a corrupted variant of the standard DVS Gesture [1] dataset. This variant introduces six distinct corruption types: DropPixel, DropEvent, RefractoryPeriod, TimeJitter, SpatialJitter, and UniformNoise. These corruptions, implemented via the Tonic API [29], effectively simulate real-world imperfections in event-based data, including sensor noise and timing inaccuracies.

D.2 More Details on Pretrained Models

SNN-VGG with BNNTT We adopt SNN-VGG with Batch-Normalization Through Time (BNNTT) [24] as our main backbone model. BNNTT decouples the parameters along the time axis

within each layer, effectively capturing the temporal dynamics of spikes. The temporally evolving learnable parameters in BNNT enable neurons to regulate their spike rates across different time steps, facilitating low-latency and low-energy training from scratch. The pre-trained model achieves accuracies of 90.61%, 69.50% and 58.36% on the original CIFAR-10, CIFAR-100 and Tiny-ImageNet test sets respectively.

SNN-ResNet To explore other CNN architecture, we use SNN-ResNet11 [27], which trains SNNs directly via surrogate gradient. The pre-trained model used in our experiments can achieve 90.95% accuracy on the original CIFAR-10 test sets.

Spike-driven Transformer V3 To evaluate the effectiveness of our work on more complex networks and datasets, we utilized a 19M parameter model in Spike-driven Transformer V3 [44], which achieves 79.60% accuracy on the ImageNet-1K validation set. This model has a patch size of 14×14 , with an embedding dimension of 360 output by the final feature extractor. Instead of using the class token, the entire embedding feature map is employed as the input to the classifier. This design naturally aligns with our method, where the channel dimension C corresponds to the embedding dimension, and the spatial dimension D matches the patch size.

SNN-ConvLSTM DVS Gesture is a neuromorphic dataset with a temporal dimension, making it well-suited for evaluating RNN-based architectures. To validate the effectiveness of our work on such networks, we employed a spike-driven 2ConvLSTM-1FC model, with hidden layer dimensions of 32 and 64, respectively. This network achieves an accuracy of 93.36% on the original DVS Gesture test set.

D.3 More Details on Implementation

To better reflect real-world scenarios, we adapt our method to independently perform adaptation on each individual test input. In the same experiment, the learning rate remains fixed across different shifted domains, as the domain of a given test sample is typically unknown in real-world settings. For each set of experiments, we employ the SGD optimizer and evaluate learning rates ranging from 0.001 to 0.8, selecting the optimal value based on performance. We trained and tested all models and datasets in 4 NVIDIA GeForce RTX 3090 GPUs.